

5-33
167-5
P-17

Experimental and Modal Verification of an Integral Equation Solution for a Thin-Walled Dichroic Plate With Cross-Shaped Holes

L. W. Epp

Radio Frequency and Microwave Subsystems Section

P. H. Stanton

Ground Antennas and Facilities Engineering Section

In order to add the capability of an X-band uplink onto the 70-m antenna, a new dichroic plate is needed to replace the Pyle-guide-shaped dichroic plate currently in use. The replacement dichroic plate must exhibit an additional passband at the new uplink frequency of 7.165 GHz, while still maintaining a passband at the existing downlink frequency of 8.425 GHz. Because of the wide frequency separation of these two passbands, conventional methods of designing air-filled dichroic plates exhibit grating lobe problems. A new method of solving this problem by using a dichroic plate with cross-shaped holes is presented and verified experimentally.

Two checks of the integral equation solution are described here. One is the comparison to a modal analysis for the limiting cross shape of a square hole. As a final check, a prototype dichroic plate with cross-shaped holes was built and measured.

I. Introduction

The unit cell shape of a thick frequency selective surface, or dichroic plate, is dependent on its frequency requirements. One aperture shape may be chosen to give wider bandwidths, and another may be chosen for sharper frequency roll-off. This is analogous to circuits where the need for differing frequency responses determines the circuit topology.

Acting as spatial frequency filters, dichroic plates are a critical component in providing the DSN spacecraft command and control uplinks as well as spacecraft downlinks.

Currently these dichroic plates separate the S-band at 2.0–2.32 GHz from the X-band at 8.4–8.45 GHz. But new spacecraft communication requirements are also calling for an uplink frequency at 7.165 GHz. Even more frequency demands are being placed on the dichroic plates being designed and built for the new beam-waveguide antennas. Future spacecraft will require these dichroic plates to effectively separate Ka-band frequencies in the 31–35 GHz range.

The requirements for these dichroic plate surfaces are low transmission loss of <0.1 dB at high power levels, and a minimal relative phase shift between polarizations for

circular polarization transmission. Even in the past, these demanding requirements caused the dichroic plate designs to change from circular apertures to Pyle apertures.¹ Currently the dichroic plate used on the 70-m antenna in the DSN consists of Pyle-shaped apertures/waveguides, see Fig. 1. Originally this plate began with a design for normal incidence using circular holes. When the circular-hole plate was measured at the desired 30-deg incident angle, the resonant frequencies for the two orthogonal polarizations had been shifted. As a first correction, the calculated electrical lengths of a Pyle guide at 8.425 GHz were set equal to the electrical lengths of the circular guide at the two measured resonance frequencies. The plate was then rebuilt with Pyle-shaped apertures.

More current work has shown the successful demonstration of design techniques for straight, rectangular apertures at an incident angle of 30 deg [1]. Rectangular apertures offer a slight design advantage in terms of packing density over the Pyle aperture plate, and therefore may give improved performance at wider angles of incidence. Wide-angle performance is a consideration in practice where the dichroic plate is excited at angles other than the nominal 30 deg due to feed horn effects. For example, a 22-dB horn pattern can have considerable power in other plane waves incident in the range of 30 deg \pm 15 deg [2].

Grating lobes are the excitation of higher-order Floquet harmonics that transmit and reflect power at angles other than the incident angle. They become a consideration when the bandwidth required to include the new frequency of 7.165 GHz conflicts with the desired incident angle of 30 deg and the operation at the higher frequency band of about 8.425 GHz. In order to design a suitable dichroic plate with rectangular or Pyle-guide apertures, the aperture dimensions must be large enough to be above cutoff for the lower frequency passband. Even when using minimal wall thickness, this creates a unit cell capable of supporting grating lobes at the higher frequency passband. In addition, although dual passbands can be demonstrated with a rectangular aperture, there is not enough independent control to align the transverse electric/transverse magnetic (TE/TM) passbands as shown in Fig. 2. In contrast, Fig. 2 shows that the cross shape's more independent passband control makes dual passbands possible.

Because of the cross shape's increased packing density, grating lobes are pushed out to wider angles of incidence.

¹ P. D. Potter, *Improved Dichroic Reflector Design for the 64-Meter Antenna S- and X-Band Feed Systems*, JPL Technical Report 32-1526 (internal document), vol. 19, Jet Propulsion Laboratory, Pasadena, California, pp. 55-62, February 15, 1974.

One method, proposed by Ootshi and Franco [3], of eliminating the grating lobe problems of the Pyle-shaped apertures was to fill them with Teflon dielectric material. The dielectric constant of 2.04 would allow the holes to be smaller, and therefore to be packed more closely together. Somewhat difficult to manufacture, the Teflon dielectric plugs were placed in liquid nitrogen and then allowed to expand into the holes of the dichroic plate, with an unknown effect on the dielectric constant. Their computer analysis showed that the dielectric constant needed to be known to an accuracy of better than 5 percent. Any change in the dielectric constant affects the desired plates thickness.

Prototypes for this type of dielectric-filled dichroic plate showed that if fabrication difficulties could be overcome, the loss tangent of the Teflon contributed an additional 1.3 K of noise temperature. With uplink frequency powers in excess of 100 kW, the question of arcing at improperly filled interfaces due to the high power levels was raised by Ootshi and Franco [3]. Lossy dielectric materials could also pose a power dissipation problem. Thus it is clearly desirable to find an air-filled dichroic plate solution that would be superior in power dissipation, power handling, and noise temperature considerations.

II. The Dichroic Plate With Cross-Shaped Holes

In order to duplex the S- and X-bands (the downlink at 8.425 GHz and the new uplink of 7.165 GHz), cross-shaped apertures in a dichroic plate have been investigated. Figure 3 shows the geometry and gives the prototype dimensions. The analysis consisted of an integral equation method of moments solution [4,5]. This method solves for the currents along the walls inside the cross, including those along the hole depth in the z direction.

Integral equation methods can be extended to handle wall thickness, but the model used here consists of a thin-walled cross on a skewed grid. Validation for using the thin-wall model comes from the need to minimize grating lobe behavior at the higher frequency band of operation. Therefore, the unit cell size must be kept to a minimum, which implies that the wall thickness too should be minimized.

A. Modal Analysis of the Limiting Shape of the Square Hole

The unit cell of the dichroic plate with cross-shaped holes on an irregular grid consists of six vertical plates as shown in Fig. 4. The current continuity between unit cells is enforced by the currents J_1 and J_2 shown. The

flexibility of this analysis is that any other shape that can be constructed of vertical plates can also be analyzed, such as the honeycomb [5].

In the modal analysis of a dichroic plate problem, this flexibility is not present, since the modes of the waveguides (repeated periodically in the dichroic plate) change as the waveguide shape changes. Modal analysis is further complicated for waveguide shapes such as the cross-shaped waveguide, where simple analytical formulations of the waveguide modes do not exist. By expansion in suitable eigenfunctions and numerical solution using the Ritz-Galerkin method, Lin solved for the modes of the cross-shaped waveguide [6]. Another method for finding the modes of the cross includes the finite element method as demonstrated by Stalzer et al. [7]. Using the modes found by Lin [6], a modal analysis of a dichroic plate with cross-shaped holes on a regular grid was developed by Compton et al. [8].

To check the accuracy of the integral equation solution in this work for an irregular or skewed grid, a limiting case of the cross waveguide was chosen. By setting $b_x = 0$, the analysis becomes that of a square hole, which can be compared to the modal analysis of Chen [1]. A good estimate of the error from the thin-wall approximation can be made from the modal analysis of the square hole.

The integral equation solution uses a first-order spatial domain Green's function evaluation [4,5,9]. The Green's function for the electric field integral equation (EFIE) is given by

$$G_p = (G_p - G^a) + F^{-1} (\tilde{G}^a) \quad (1)$$

where the spatial domain Green's function is given by

$$G_p(\vec{r}_0, \vec{r}') = \sum_{m=-\infty}^{m=+\infty} \sum_{n=-\infty}^{n=+\infty} e^{-j\vec{k}_0 \cdot \vec{\rho}_{mn}} \frac{e^{-jk_0 \sqrt{|\vec{\rho}_0 - \vec{\rho}' - \vec{\rho}_{mn}|^2 + (z_0 - z')^2}}}{4\pi \sqrt{|\vec{\rho}_0 - \vec{\rho}' - \vec{\rho}_{mn}|^2 + (z_0 - z')^2}} \quad (2)$$

The spatial lattice translation vector needed is defined by

$$\vec{\rho}_{mn} = (nd \cos \Omega) \hat{x} + (mc + nd \sin \Omega) \hat{y} \quad (3)$$

and Fig. 4 defines the distances c and d as well as the skew angle Ω . The corresponding asymptotic Green's function used was

$$G_p(\vec{r}_0, \vec{r}') = \sum_{m=-\infty}^{m=+\infty} \sum_{n=-\infty}^{n=+\infty} e^{-j\vec{k}_0 \cdot \vec{\rho}_{mn}} \frac{e^{-jk_0 \sqrt{|\vec{\rho}_0 - \vec{\rho}' - \vec{\rho}_{mn}|^2 + (|z_0 - z'| + cCA)^2}}}{4\pi \sqrt{|\vec{\rho}_0 - \vec{\rho}' - \vec{\rho}_{mn}|^2 + (|z_0 - z'| + cCA)^2}} \quad (4)$$

The cell area needed in the asymptotic form of spectral domain Green's function

$$G_p(\vec{r}_0, \vec{r}') = \frac{1}{\text{cell area}} \sum_{m=-\infty}^{m=+\infty} \sum_{n=-\infty}^{n=+\infty} \frac{e^{-j\gamma|z_0 - z'| + cCA} e^{j(\vec{K}_{mn} - \vec{k}_0) \cdot (\vec{\rho}_0 - \vec{\rho}')}}{2j\gamma} \quad (5)$$

is the area enclosed inside the unit cell shown in Fig. 4 where

$$\vec{K}_{mn} = 2\pi \left[\frac{n}{d \cos \Omega} - \frac{m \sin \Omega}{c \cos \Omega} \right] \hat{x} + \frac{2\pi m}{c} \hat{y} \quad (6)$$

When the basis and testing functions used in the EFIE method of moments (MOM) solution do not overlap in the z direction, the spatial acceleration shown in Eq. (1) is not used. Instead, it is replaced by the spectral domain Green's function found from Eq. (5) by letting $cCA = 0$.

From the spectral domain Green's function, it is seen that the Floquet harmonics are described by plane wave spectral components propagating according to

$$\gamma = \begin{cases} \sqrt{k_0^2 - \beta_{xmn}^2 - \beta_{ym}^2} & k_0^2 > \beta_{xmn}^2 + \beta_{ym}^2 \\ -j\sqrt{\beta_{xmn}^2 + \beta_{ym}^2 - k_0^2} & \beta_{xmn}^2 + \beta_{ym}^2 > k_0^2 \end{cases} \quad (7)$$

and

$$\beta_{xmn} = (\vec{K}_{mn} - \vec{k}_0) \cdot \hat{x} = 2\pi \left[\frac{n}{d \cos \Omega} - \frac{m \sin \Omega}{c \cos \Omega} \right] - k_x \quad (8)$$

$$\beta_{ym} = (\vec{K}_{mn} - \vec{k}_0) \cdot \hat{y} = \frac{2\pi m}{c} - k_y \quad (9)$$

The phase shift from cell to cell is determined by the phase shifts of the incident plane wave

$$\begin{aligned} k_x &= -k_0 \sin \theta_i \cos \phi_i \\ k_y &= -k_0 \sin \theta_i \sin \phi_i \\ k_z &= -k_0 \cos \theta_i \end{aligned} \quad (10)$$

The modal analysis uses rectangular waveguide modes inside the rectangular holes, matched to Floquet modes at the apertures. Formulations for the Floquet modes can be found in [2] and will not be included here. But of importance is the number of Floquet modes chosen in relationship to the number of rectangular waveguide modes. In comparison to the integral equation method, it was necessary for convergence to increase the number of waveguide modes. If $mmax$ and $nmax$ represent the highest waveguide mode indices used, the Floquet modes m and n were chosen so that

$$\begin{aligned} \beta_{xmn} &\approx \frac{(mmax)\pi}{H_x} \\ \beta_{ym} &\approx \frac{(nmax)\pi}{H_y} \end{aligned} \quad (11)$$

and then incremented by three.

Figure 5 shows the geometry of the square-hole test case. For initial comparison to the thin-wall integral equation solution, the dimensions were $H_x = H_y = S_x = S_y = 2.59$ cm. The definitions of the two incident polarizations used are shown in Fig. 6. Figures 7 and 8 show the comparison of the two solutions for normal incidence. The TE polarization shows a maximum error of 0.66 percent and the TM polarization shows twice as much error, or 1.33 percent. For completeness, the phase comparisons of these two test cases are shown in Figs. 9 and 10.

The modal solutions convergence is affected by the number of rectangular waveguide modes used. In the analysis of Figs. 7–10, the number of rectangular waveguide modes used was 220. The convergence of the resonant locations for the modal analysis is shown in Fig. 11. The number of basis functions used along the depth of the holes for the integral equation solution was 30. It too is sensitive to the number of basis functions used, as shown in Fig. 12. Besides the discretization error, other possible sources of error exist, and it should be noted that no attempt was made to match the proper edge behavior for a thin wall in the modal solution.

For plate rigidity, the prototype plate was designed with a wall thickness of 0.041 cm. Therefore, an inherent error in this analysis is the effect of this wall thickness. A good estimate of this error can be made from the modal analysis of the square hole. Figures 13 and 14 show the modal analysis of the square hole where the wall thickness of the prototype is changed from a thin wall to one of a width of 0.041 cm. Both Figs. 13 and 14 were made for normal incidence, which differs from the 30-deg incident angle of the prototype plate. Note that Figs. 13 and 14 show the analysis when the wall thickness has been added in such a way as not to change the periodicity of the unit cell, $H_x = H_y = 2.55$ cm and $S_x = S_y = 2.59$ cm. The thin wall solution has dimensions $H_x = H_y = S_x = S_y = 2.59$ cm. The error for the TE polarization is 0.44 percent and the error for the TM polarization is 0.55 percent.

When the wall thickness is added in such a way as to change the periodicity of the structure, a more dramatic shift in the resonant location of each polarization occurs. Figures 15 and 16 show the results when $H_x = H_y = 2.59$ cm and $S_x = S_y = 2.63$ cm. Here the error increases from 0.44 percent to 1.33 percent for the TE polarization and from 0.55 percent to 1.44 percent for the TM polarization. This implies that to minimize the effect of the wall thickness in the integral equation solution for the cross shape, it should be added in such a manner as not to change the periodicity. Note here that changing the periodicity of the

square-hole shape significantly lowered the frequency of the resonant locations.

B. Integral Equation Design of Prototype S-/X-Band Dichroic Plate With Cross-Shaped Holes

For the prescribed angle of incidence $\theta = 30$ deg, minimum grating lobes are exhibited by the cross shape when $\phi = 0.0$ deg. The TE polarization is more affected by the cross-shape dimensions of a_x and b_x . Generally, the cross shape can be thought of as two orthogonal rectangular waveguides, one for each polarization. So the x arm of the cross can be thought of as a rectangular waveguide that transmits the TE polarization. The TM polarization is more affected by the y arm of the cross shape. Of course, because of the exact shape of the cross waveguide, one polarization will couple to the other. But because the two polarizations are only weakly coupled, a useful design that optimizes the performance of both bands can be made.

The results for an air-filled, cross-shaped aperture with dimensions $a_x = 2.65$ cm, $b_x = 0.6$ cm, $a_y = 2.76$ cm, $b_y = 0.7125$ cm, an aperture depth of 3.5 cm, a skewed grid angle of $\Omega = 33.95$ deg, and an incident angle of $\theta = 30$ deg are shown in Fig. 17. Transmission results are shown in Fig. 18 and both results are summarized in Table 1. These results and dimensions were used as a basis for the prototype dimensions. The number of basis functions used in discretizing the depth was 12.

Because cross-shaped apertures pack more tightly than rectangular apertures, it is possible to obtain a dichroic plate with the desired dual X-band passbands grating lobe free. In contrast, this could not be done with the air-filled rectangular shape without the introduction of grating lobes because the minimum unit cell size is the size of the aperture. The more tightly packed cross-shaped elements overlap in the x direction, reducing the unit cell size in the x direction to less than the length of the cross arm a_x .

This design also gives a minimum phase shift between the two transmitted polarizations at the more critical downlink frequency of 8.425 GHz. The phase difference at the downlink frequency is small, 2.93 deg, but the trade-off is a phase difference at the uplink of 16.9 deg, as shown in Fig. 19. If more phase shift is allowed at the uplink frequency, which could be compensated for by a polarizer, a slightly different design may allow for slightly more bandwidth.

III. Grating Lobe Study

For a dichroic plate, a grating lobe is due to the propagation of a higher-order Floquet harmonic other than the

zeroth order $m = n = 0$ harmonic. The zeroth-order Floquet harmonic is usually of interest because it satisfies Snell's law for reflection and transmission. In other words, the angles of transmission and reflection are equal to the angle of incidence. The current design dimensions give a plate that will be grating lobe free to $\theta = 44$ deg at $\phi = 0$ deg (i.e., from the more tightly packed x direction) and frequency of 8.625 GHz. Figure 20 shows the results of the preliminary cross-shape design with the incident angles of a 22-dB feed horn transformed to the coordinates of the dichroic plate as done by Chen [2]. The curve marked maximum theta (Θ) is the maximum incident angle that a plane wave can strike this dichroic plate before grating lobes are produced.

IV. Experimental Verification and Analytical Improvements

The aluminum test plate was constructed using wire electrical discharge machining from an aluminum sample of 39.4 cm by 39.4 cm. The overall plate consisted of 213 holes, covering an internal area of approximately 36.2 cm by 36.2 cm. Figure 21 shows the mechanical drawing for the prototype plate. Note that the dimensions are slight modifications of the above preliminary design to allow for an addition of 0.041 cm of wall thickness. Figure 22 shows the partially completed prototype, and Fig. 23 shows a close-up of the cross-shaped holes.

The measured interior dimensions of the cross-shaped waveguide composing the prototype were measured to be $a_x' = 2.64744$ cm, $b_x' = 0.60008$ cm, $a_y' = 2.75742$ cm, $b_y' = 0.70021$ cm, and the hole depth was 3.35 cm. A comparison of these measured values with those given in Fig. 21 shows that a tight manufacturing tolerance was held as all internal cross dimensions were decreased consistently by 0.0254 cm. This very slight shortening of all interior dimensions was reflected in wall thickness and not in the distance between the centers of the holes. The only fabrication error was a slight shift in the centers of one row of cross-shaped holes of approximately 0.0254 cm.

Figure 24 shows the experimental results, while Figs. 25 and 26 show the initial computed results before making improvements. The computed results use the interior dimensions of the cross-shaped waveguide and the incident angle of $\theta = 30$ deg and $\phi = 0.0$ deg. The number of basis functions used to discretize the depth was 12, which was clearly insufficient.

As mentioned in the comparison of the modal analysis, it is necessary to use the exterior cross dimensions so

that the periodicity of the theoretical model is the same as in the prototype. Adjusting for the wall thickness in this manner, the measured values give $a_x = 2.69047$ cm, $b_x = 0.60008$ cm, $a_y = 2.80004$ cm, and $b_y = 0.70021$ cm. The skew grid angle of the theoretical calculations becomes the correct $\Omega = 33.81$ deg of the prototype. After making accuracy improvements to the theoretical calculations along with this adjustment of dimensions, the comparison to computed results is shown in Figs. 27 and 28.

Improvements to the theoretical analysis consisted of two parts, one geometric and one analytic. The geometric improvements came from realizing that there is a correct way to adjust the theoretical dimensions that were determined by comparison with the limiting case of the square-hole shape. This was demonstrated in Figs. 15 and 16.

One analytical improvement consisted of increasing the sampling density of the currents along the wall. This allows the current to be modeled more accurately in rapidly varying areas like the edges of the plate and around the 90-deg bends on the inside of the cross. This proved to be more important in discretizing the depth of the dichroic plate, as the current discretization uses a pulse approximation to triangle basis functions that are sampled at a point just inside the length of the dichroic plate. This leads to a small length error which can be compensated for, and decreases as the sampling density is increased.

Increasing the sampling density also allows the resonant frequencies to converge to their true value. This was demonstrated by Fig. 12, where it was seen that the resonant frequency locations were seen to be still converging for 27 basis functions per wavelength. In the case of the cross shape, the number of basis functions along the length of the cross was varied until the resonant frequencies changed to less than 0.01 GHz. For the results of Figs. 27 and 28, a total of 30 basis functions was used to discretize the depth, except immediately around the resonant loca-

tions where, for increased accuracy, 36 basis functions were used.

The second set of analytical improvements came from replacing the approximation to the periodic spatial domain Green's function being used in the first term of Eq. (1). Unfortunately this approximation was implemented in order to make the solution more computer efficient [5]. This approximation amounts to limiting the mutual coupling effects of each cross hole to its nearest neighbors and sums the contributions for $m, n = -1, 0, 1$. This was replaced with a summation that was then summed to the same specified accuracy as the spectral Green's function term. Again these parameters were increased until the resonant frequencies changed to less than 0.01 GHz. This doubled the computation time.

A summary of the error for the cross-shaped test plate is given in Table 2.

The conductivity loss has not yet been calculated. An advantage of this method is that the conductivity loss is present in the theoretical model. In the past, conductivity loss has been estimated based on the assumption of a dominant TE_{10} (square) waveguide mode [2]. This loss can be calculated as a function of frequency, and its impact on the transmission loss can be found.

V. Conclusions

A detailed analysis of a cross-shaped dichroic plate has been presented that shows dual passbands in the transmission region. As a check on the analysis used on the cross shape, it was compared to the modal analysis for the special case of the square hole. The modal analysis of the square hole was used to determine the effect of the modelling error of the thin-wall approximation used in the cross shape. As a final check on the analysis for the cross shape, the construction and testing of a cross-shaped dichroic plate prototype have been described.

Acknowledgments

The authors thank Jacqueline C. Chen for providing the modal analysis programs and Harry Reilly, Jr., for taking care of all the manufacturing details of the prototype plate. The authors also acknowledge the integral equation programs provided by Roy E. Jorgenson of Sandia National Laboratories and Professor Raj Mittra of the University of Illinois, which formed the basis of the cross analysis, making this work possible.

References

- [1] J. C. Chen, "Analysis of a Thick Dichroic Plate With Rectangular Holes at Arbitrary Angles of Incidence," *The Telecommunications and Data Acquisition Progress Report 42-104*, vol. October–December 1990, Jet Propulsion Laboratory, Pasadena, California, pp. 9–16, February 15, 1991.
- [2] J. C. Chen, "X-/Ka-Band Dichroic Plate Design and Grating Lobe Study," *The Telecommunications and Data Acquisition Progress Report 42-105*, vol. January–March 1991, Jet Propulsion Laboratory, Pasadena, California, pp. 21–30, May 15, 1991.
- [3] T. Y. Otoshi and M. M. Franco, "Dual Passband Dichroic Plate for X-Band," *The Telecommunications and Data Acquisition Progress Report 42-94*, vol. April–June 1988, Jet Propulsion Laboratory, Pasadena, California, pp. 110–134, August 15, 1988.
- [4] R. E. Jorgenson, "Electromagnetic Scattering From a Structured Slab Comprised of Periodically Placed Resistive Cards," Ph.D. dissertation, University of Illinois, Urbana, Illinois, 1989.
- [5] R. E. Jorgenson and R. Mittra, "Scattering from structured slabs having two-dimensional periodicity," *IEEE Transactions on Antennas and Propagation*, vol. 39, no. 2, pp. 151–157, February 1991.
- [6] F. C. Lin, "Modal characteristics of crossed rectangular waveguides," *IEEE Transactions on Microwave Theory and Techniques*, vol. MTT-25, no. 9, pp. 756–763, September 1977.
- [7] H. J. Stalzer, Jr., M. D. Greenman, and F. G. Willwerth, "Modes of crossed rectangular waveguide," *IEEE Transactions on Antennas and Propagation*, vol. AP-24, pp. 220–223, March 1976.
- [8] R. C. Compton, R. C. McPhedran, G. H. Derrick, and L. C. Botten, "Diffraction properties of a bandpass grid," *Infrared Phys.*, vol. 23, no. 5, pp. 239–245, 1983.
- [9] R. E. Jorgenson and R. Mittra, "Efficient calculation of the free-space periodic Green's function," *IEEE Transactions on Antennas and Propagation*, vol. 38, no. 5, pp. 633–642, May 1990.

Table 1. Preliminary results for a dichroic plate with cross-shaped holes.

Frequency, GHz	Reflection, dB		Transmission, dB	
	TE polarization	TM polarization	TE polarization	TM polarization
7.065	-19.96	-18.38	-0.04	-0.09
7.165 (uplink)	-28.33	-29.19	-0.003	-0.03
7.265	-16.53	-28.72	-0.09	-0.03
8.325	-23.55	-26.09	-0.02	-0.07
8.425 (downlink)	-30.68	-43.33	-0.003	-0.06
8.525	-19.49	-25.14	-0.05	-0.08
2.1	-0.00	-0.00	-40.23	-35.24
2.3	-0.00	-0.00	-39.08	-34.06

Table 2. Summary of error for the cross-shaped prototype.

Resonance location: Polarization frequency, GHz	Initial error: Computation and measurement, %	Final error: Computation and measurement, %	Total analytical improvement: Analysis and geometry, %
TE, 7.075	1.27	0.85	0.42
TM, 7.119	0.65	1.04	-0.39
TE, 8.197	2.71	0.22	2.49
TM, 8.186	2.92	0.48	2.44



Fig. 1. Close-up of a dichroic plate consisting of Pyle apertures.

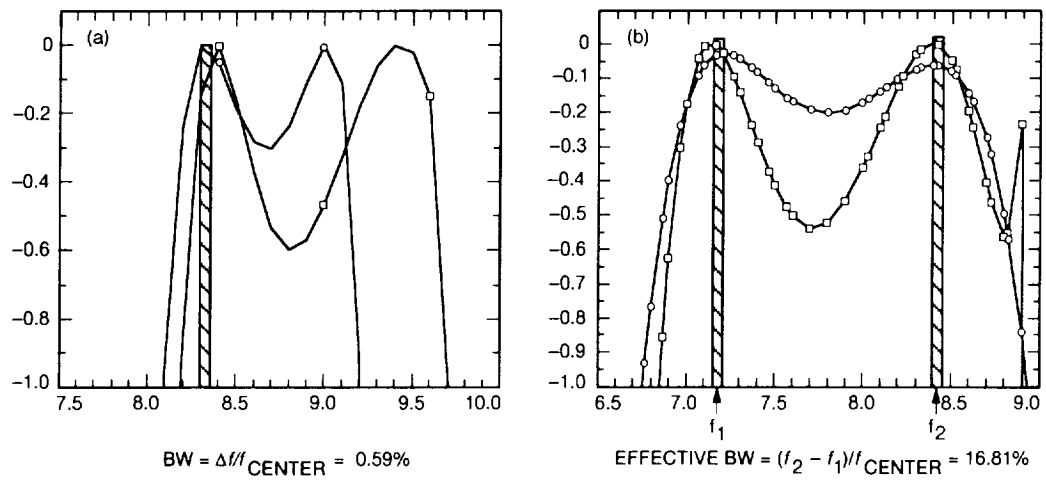
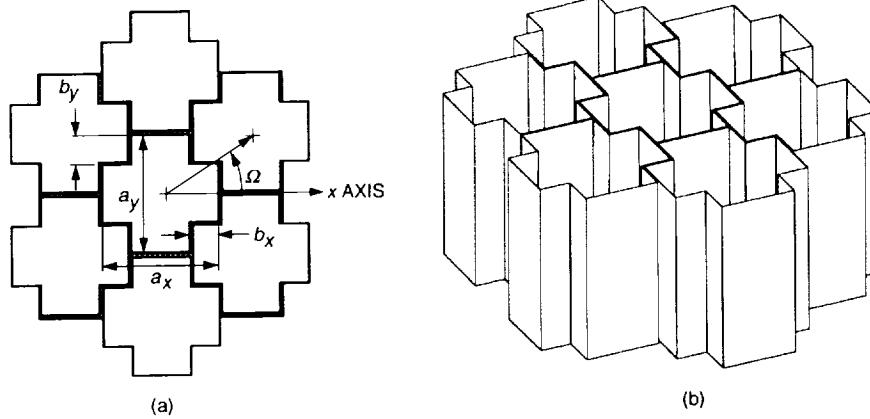


Fig. 2. Passbands of: (a) rectangular aperture, and (b) cross-shaped aperture.



PROTOTYPE DIMENSIONS: $a_x = 2.64744$ cm, $b_x = 0.60008$ cm, $a_y = 2.75742$ cm
 $b_y = 0.70021$, HOLE DEPTH = 3.35 cm
 $a_x + \text{WALL THICKNESS} = 2.69047$ cm
 $a_y + \text{WALL THICKNESS} = 2.80004$ cm

Fig. 3. Cross-shaped S-/X-band dichroic plate—prototype dimensions: (a) top view, and (b) side view.

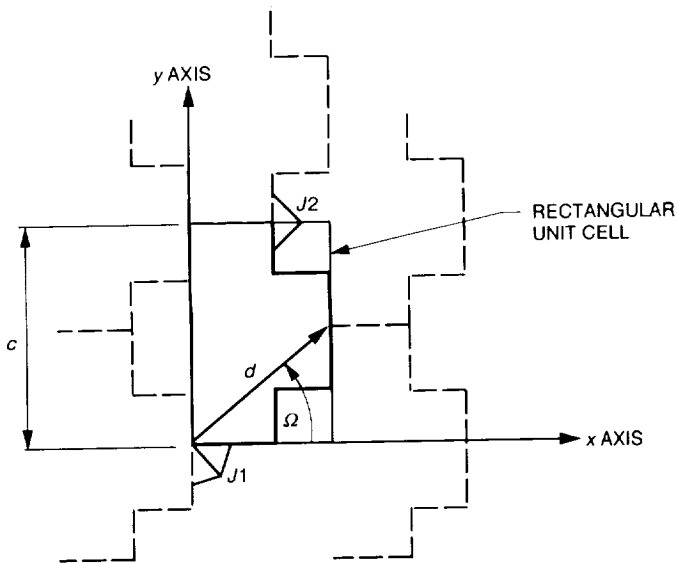


Fig. 4. Unit cell for the cross-shaped dichroic plate.

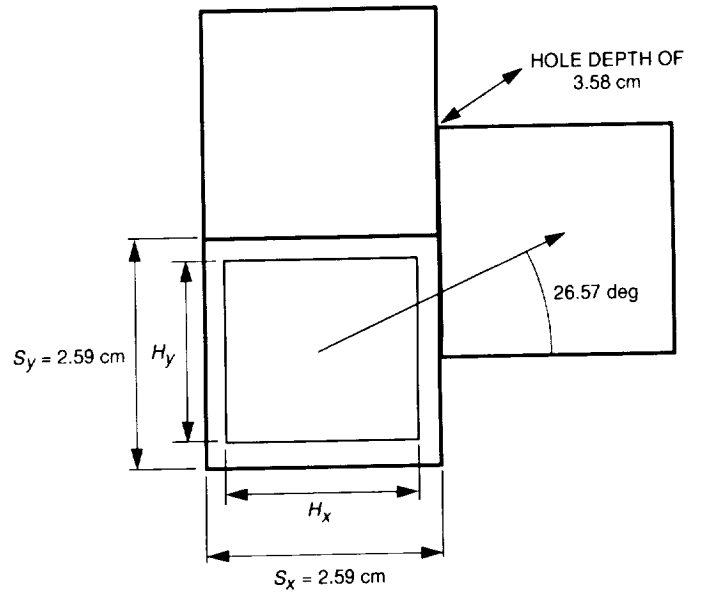


Fig. 5. Square-hole geometry.

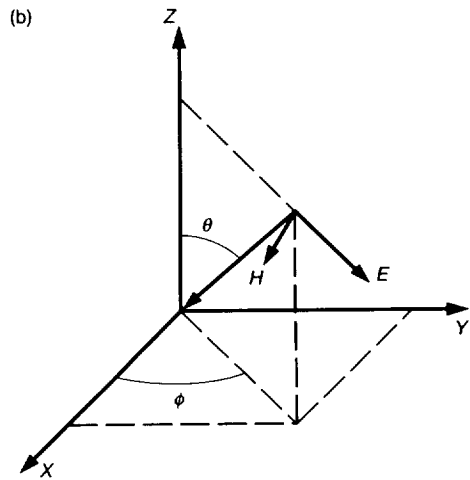
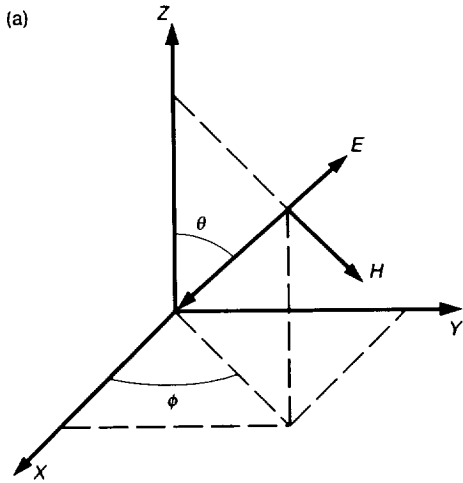


Fig. 6. Definition of two incident plane waves striking a surface in the x - y plane at the angle of θ and ϕ : (a) TE, and (b) TM.

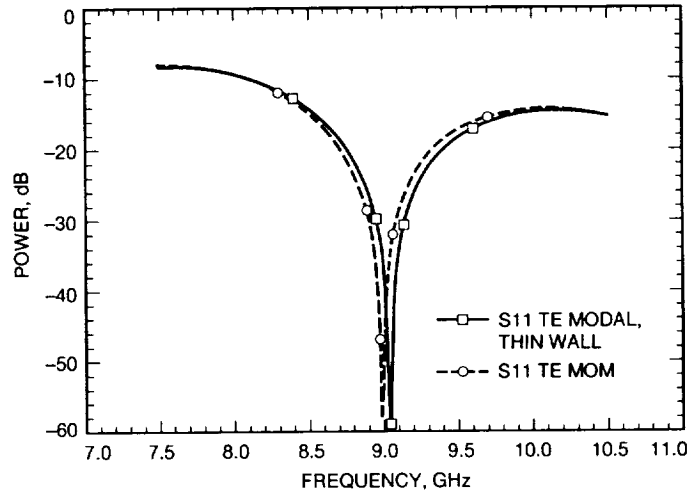


Fig. 7. Comparison of modal analysis to integral equation solution, TE polarization.

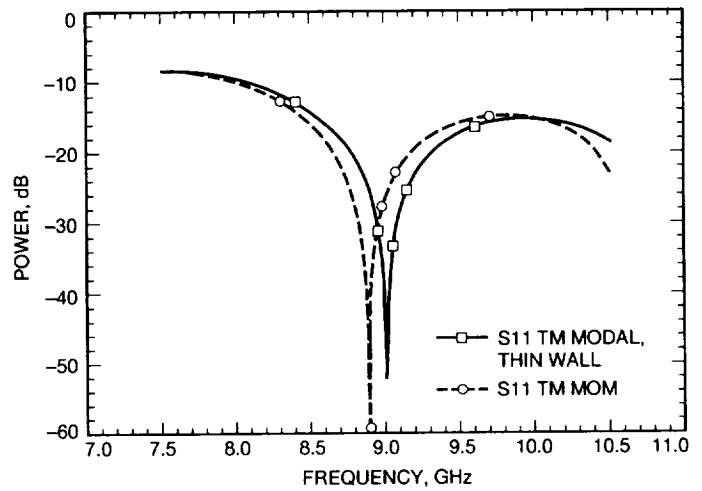


Fig. 8. Comparison of modal analysis to integral equation solution, TM polarization.

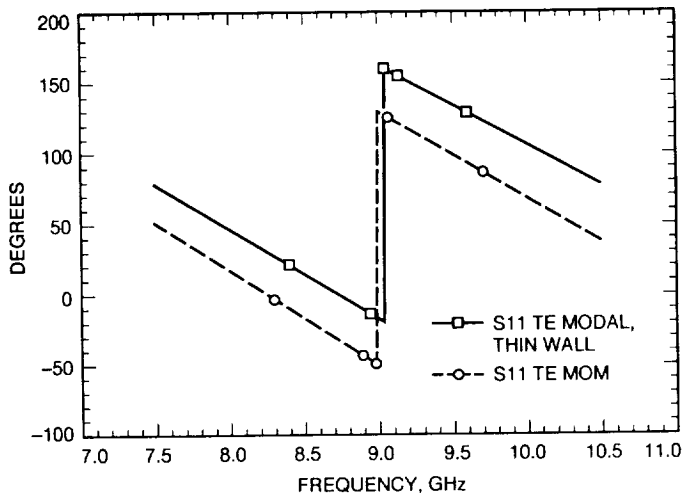


Fig. 9. Comparison of modal analysis to integral equation solution, reflected phase TE.

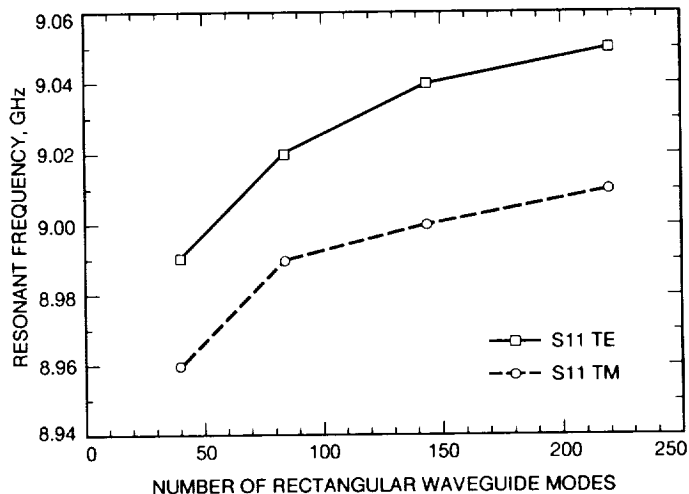


Fig. 11. Resonant frequency convergence in the modal solution of the square hole with thin walls.

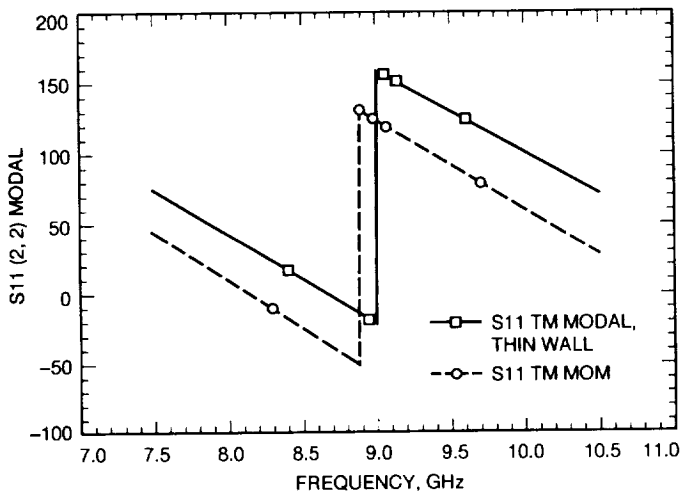


Fig. 10. Comparison of modal analysis to integral equation solution, reflected phase TM.

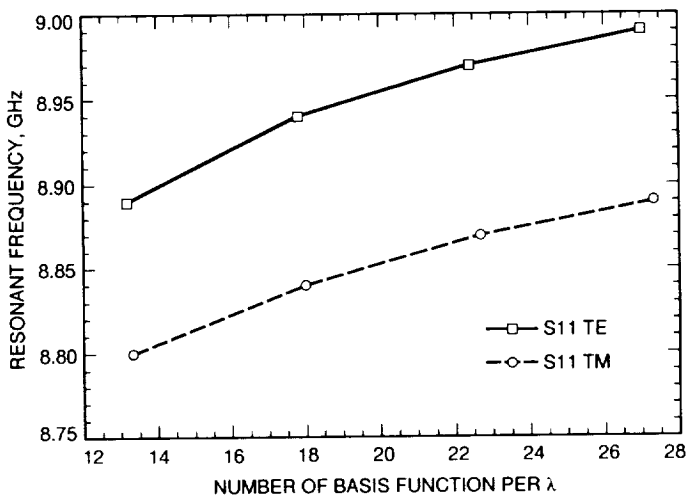


Fig. 12. Resonant frequency convergence in the method of moments solution of the square hole with thin walls.

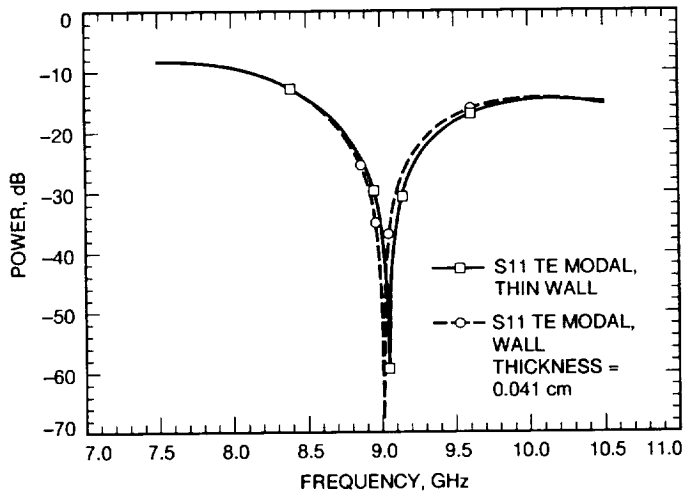


Fig. 13. Comparison of effect of wall thickness on the TE reflection coefficient.

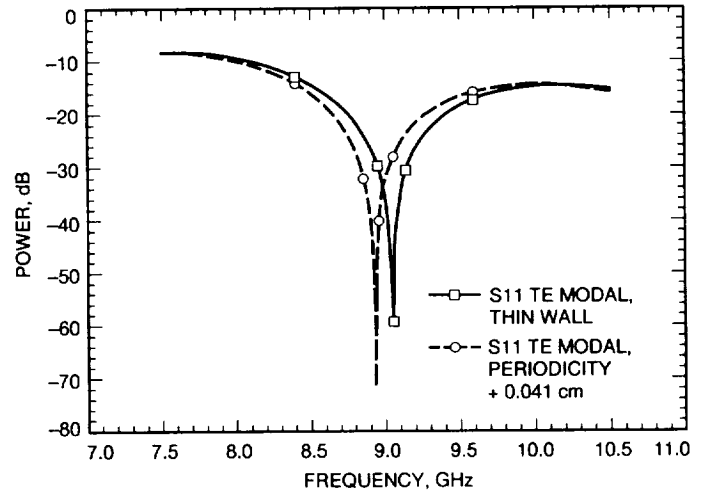


Fig. 15. Effect of periodicity change on the TE reflection coefficient.

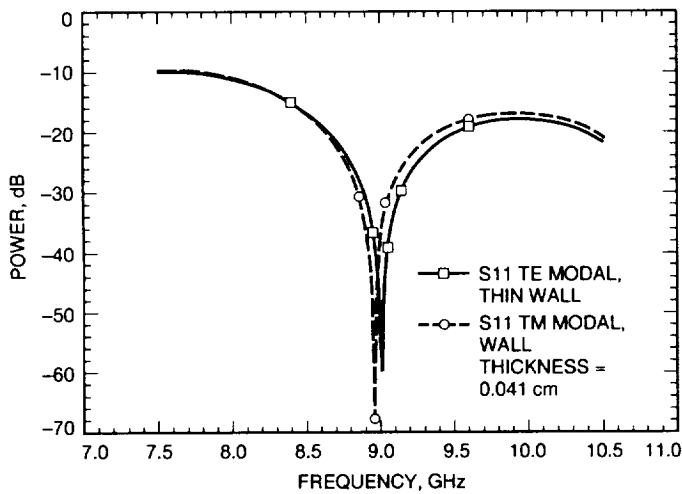


Fig. 14. Comparison of effect of wall thickness on the TM reflection coefficient.

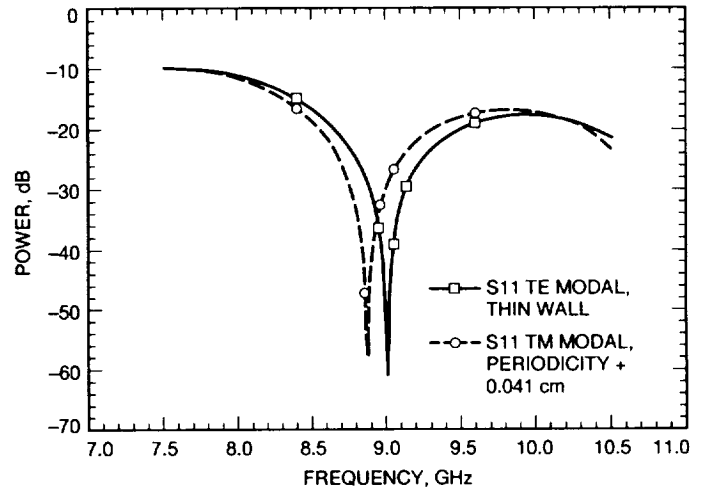


Fig. 16. Effect of periodicity change on the TM reflection coefficient.

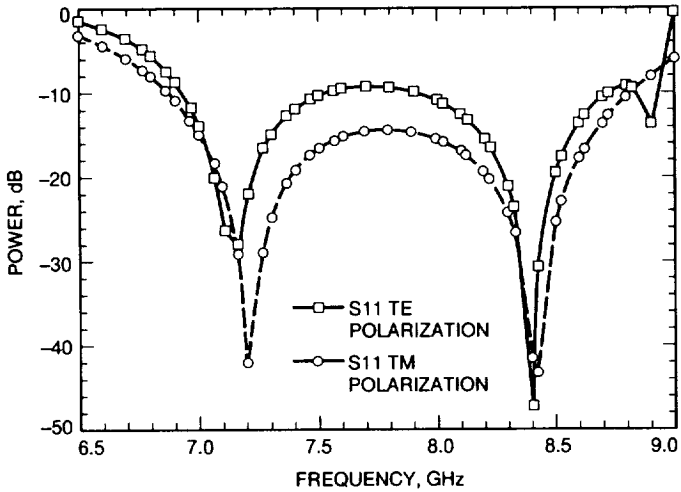


Fig. 17. Power reflection coefficient for a dichroic plate with cross-shaped holes ($a_x = 2.65$ cm, $b_x = 0.6$ cm, $a_y = 2.76$ cm, $b_y = 0.7125$ cm, depth = 3.35 cm).

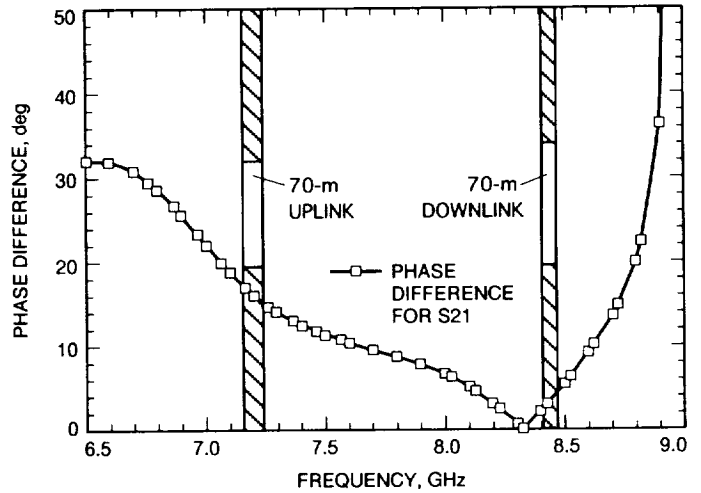


Fig. 19. Phase difference between polarizations for a dichroic plate with cross-shaped holes ($a_x = 2.65$ cm, $b_x = 0.6$ cm, $a_y = 2.76$ cm, $b_y = 0.7125$ cm, depth = 3.35 cm).

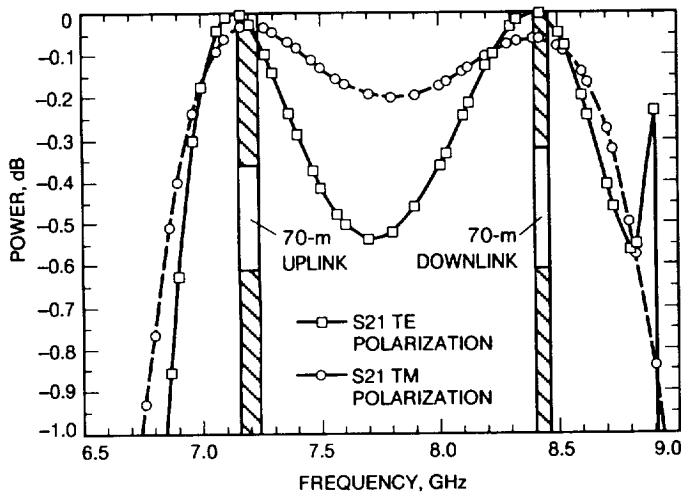


Fig. 18. Power transmission coefficient for a dichroic plate with cross-shaped holes ($a_x = 2.65$ cm, $b_x = 0.6$ cm, $a_y = 2.76$ cm, $b_y = 0.7125$ cm, depth = 3.35 cm).

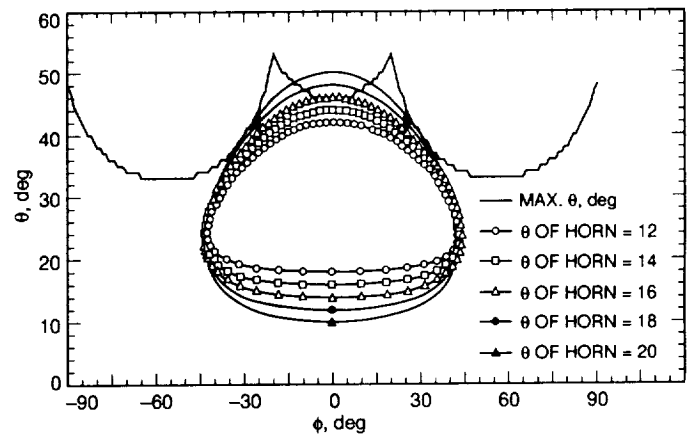
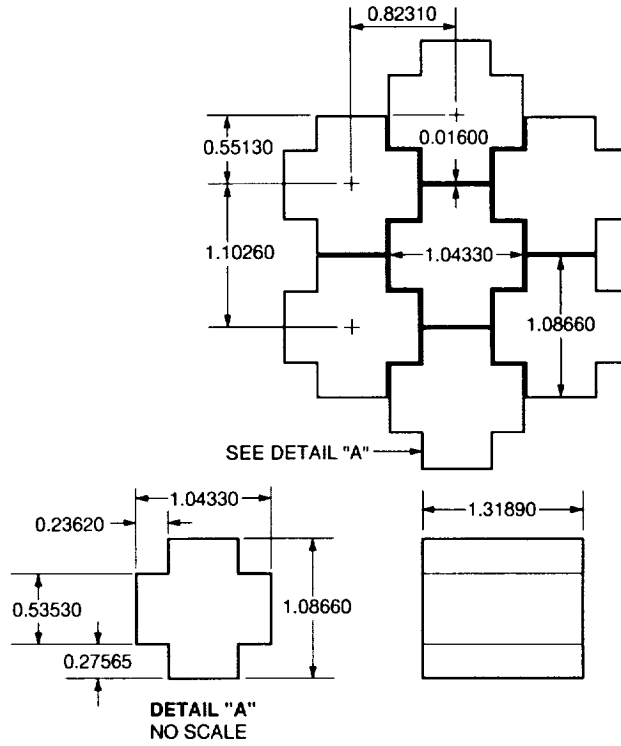


Fig. 20. Maximum angle, θ , at which a grating lobe propagates, $f = 8.625$ GHz ($a_x = 2.65$ cm, $b_x = 0.6$ cm, $a_y = 2.76$ cm, $b_y = 0.7125$ cm).



NOTE: MEASUREMENTS ARE IN INCHES

Fig. 21. Cross-shaped prototype detailed drawing.

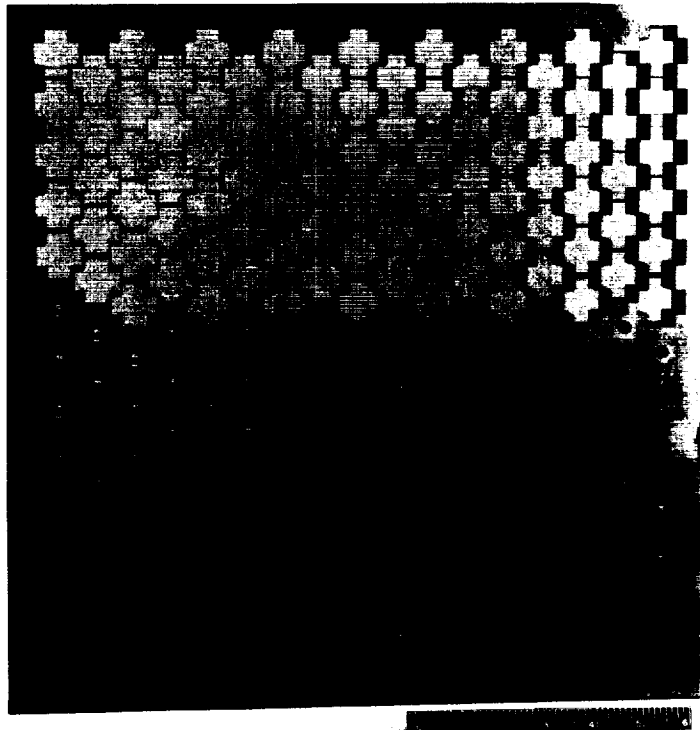


Fig. 22. Prototype of a dichroic plate with cross-shaped holes.

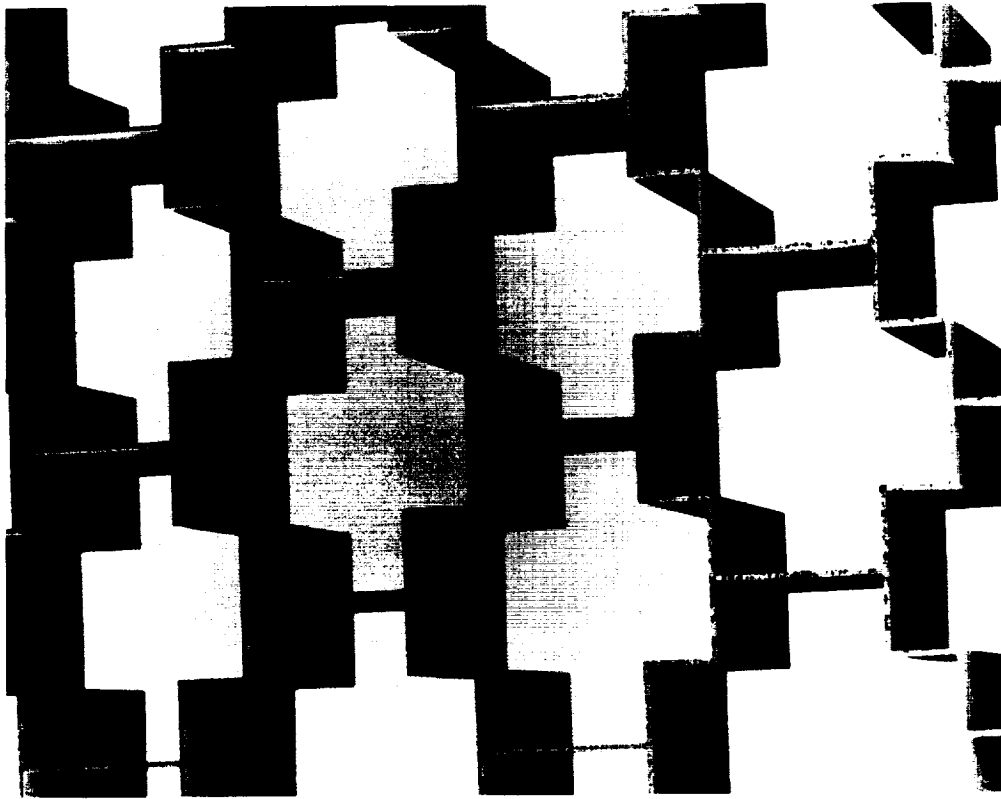


Fig. 23. Cross-shaped holes.

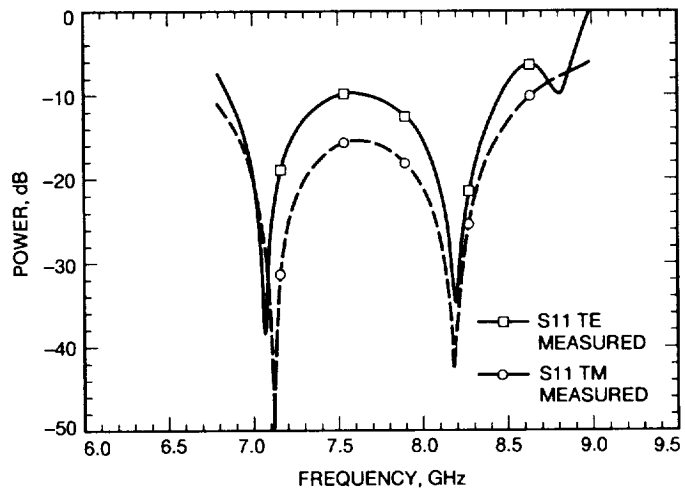


Fig. 24. Measured power reflection coefficient for a dichroic plate with cross-shaped holes.

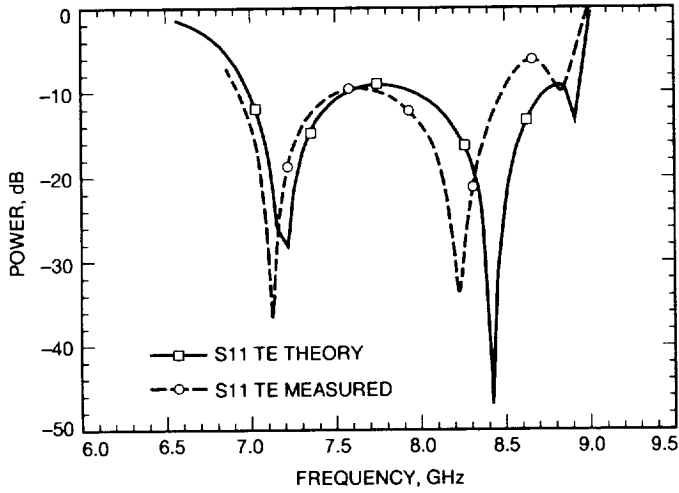


Fig. 25. Power reflection coefficient, initial comparison of measurement and theory for TE polarization.

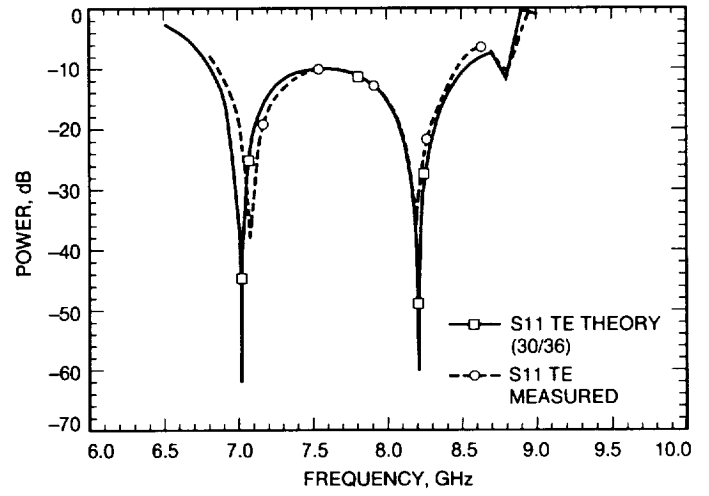


Fig. 27. Power reflection coefficient, corrected theory and measurement for TE polarization.

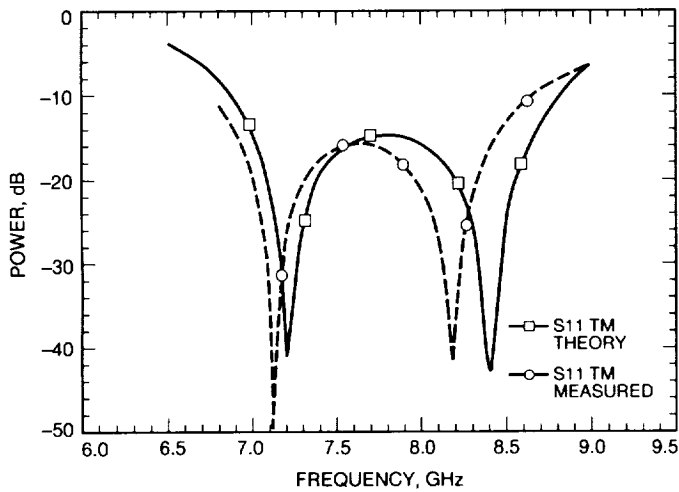


Fig. 26. Power reflection coefficient, initial comparison of measurement and theory for TM polarization.

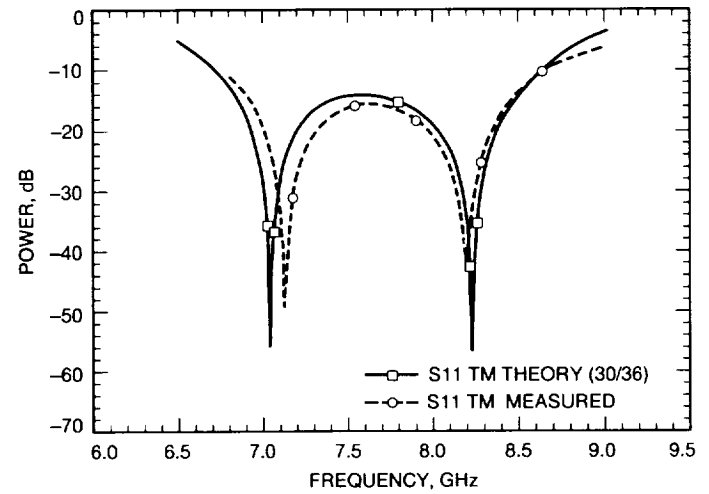


Fig. 28. Power reflection coefficient, corrected theory and measurement for TM polarization.